Joule

CellPress

Article

A high-capacity Sn metal anode for aqueous acidic batteries

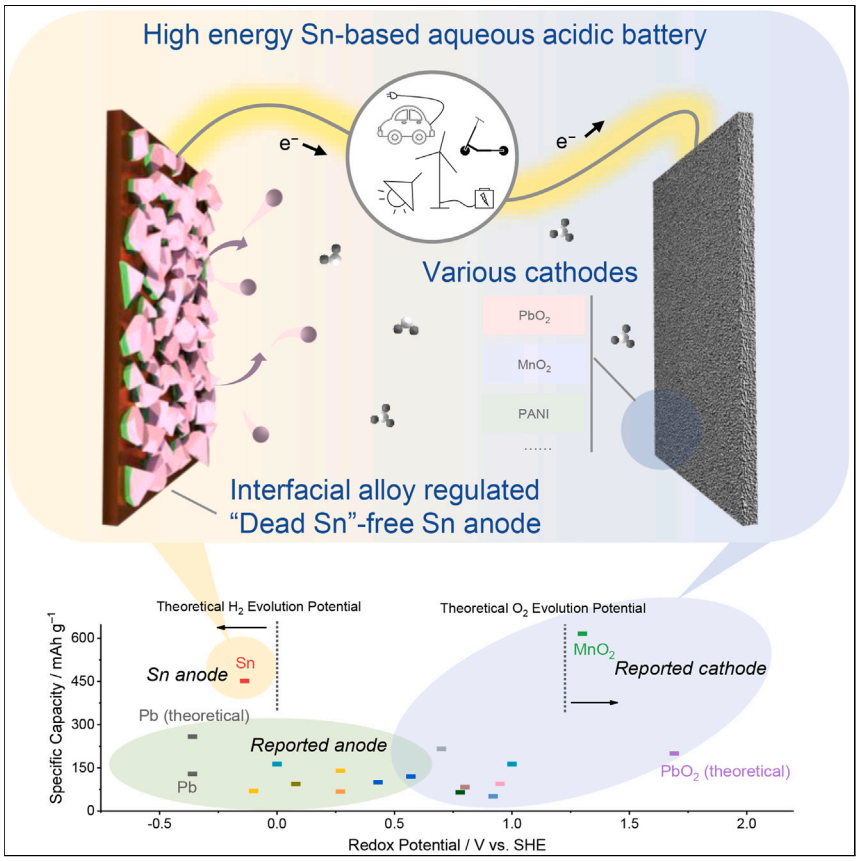

Sn metal with intrinsic advantages on capacity, redox potential, and kinetics can be well fitted into the acidic battery system as anode. Interfacial alloying regulation strategy is applied to optimize the deposition uniformity and prohibit Sn shedding during stripping/plating process, thus solving the "dead Sn" issue and improving the reversibility. With the innovation of reversible Sn anode, opportunities are provided to complete the puzzle of aqueous acidic battery construction and potentially lead to wider choices for energy storage.

Haozhe Zhang, Diyu Xu, Fan Yang, ..., Minghao Zhang, Xihong Lu, Ying Shirley Meng

luxh6@mail.sysu.edu.cn (X.L.)
shirleymeng@uchicago.edu (Y.S.M.)

Highlights

Sn metal with high capacity and low potential as qualified anode for acidic battery

"Dead Sn" issue during Sn anode cycling has been identified and solved

Interfacial alloying regulation improves deposition uniformity and reversibility

Sn anode can be matched with various cathodes and delivers good performances

Zhang et al., Joule 7, 971–985
May 17, 2023
https://doi.org/10.1016/j.joule.2023.04.011

Joule

CellPress

Article

A high-capacity Sn metal anode for aqueous acidic batteries

Haozhe Zhang,[1,2,3] Diyu Xu,[1] Fan Yang,[1] Jinhao Xie,[1] Qiyu Liu,[1] Di-Jia Liu,[2,3] Minghao Zhang,[4] Xihong Lu,[1,*] and Ying Shirley Meng[2,4,5,6,*]

SUMMARY

Aqueous acidic batteries are a good choice to respond to battery diversity, delivering safety, cost, environmental friendliness, and high-power necessary for renewable energy storage. However, the practical adoption is greatly challenged by low voltage and energy density due to the inadequate metal anode materials. Here, we report an interfacial regulated Sn metal anode as the solution of the last piece of the puzzle. The ease of recycling, low potential, fast redox kinetics, and high capacity of Sn perfectly fit the battery system, and the Sn metal shedding critical issue is successfully suppressed by promoting uniform deposition for added interaction from alloying. Consequently, this reversible Sn anode with 442 mAh g^{-1} matches well to different types of cathodes. The as-assembled acidic batteries also demonstrate sufficient output voltage (up to 1.7 V), energy density (up to 312 Wh kg^{-1} based on both electrodes), kinetics (up to 24 C), and stability (up to 2,400 cycles).

INTRODUCTION

Replacing fossil fuels with renewable energy represents a huge step forward in decarbonization.[1] The growing market penetration of renewable but intermittent energy sources such as wind and solar has generated critical needs for inexpensive, safe, and long-lasting electrochemical energy storage technologies.[2–4] Widely used lithium batteries are facing increasingly more challenges due to the usage of toxic, flammable organic electrolytes and scarce electrode materials.[5–7] As an alternative, aqueous acidic batteries (AABs) have the advantages over lithium batteries in many applications for being low cost, non-flammable, and easy to handle.[8] Compared with well-developed aqueous metallic ion batteries, AABs with non-metallic hydrated proton charge carriers are expected to deliver higher energy and faster kinetics due to light weight, low carrying charge, and no need to dehydrate hydrated protons.[9,10] These features led to development of diverse AABs (lead-acid,[11] Mn-H_2,[12] proton batteries,[13,14] metal-proton batteries,[15] etc.) with broad application prospects in both large-scale energy storage systems and daily use scenarios, such as electric scooters. Major breakthroughs in cathode materials have increased application potential of AABs. Recently, electrolytic MnO_2 cathode with high-kinetic Mn^{4+}/Mn^{2+} chemistry doubled its theoretical capacity (308 vs. 616 mAh g^{-1}) and achieved a higher redox potential (1.23 V vs. SHE, standard hydrogen electrode) compared to one electron reaction MnO_2 electrode.[16] Prussian blue analogue cathode like $Cu[Fe(CN)_6]_{0.63}\cdot\square_{0.37}\cdot 3.4H_2O$ based on proton (de)intercalation had been proposed as a super-high-rate electrode, which could even maintain half capacity

CONTEXT & SCALE

The development of diverse next-generation battery technologies is highly required by decarbonized society to better utilize renewable energy. Aqueous acidic batteries with hydrated proton charge carriers are expected to deliver high energy and fast kinetics while being inexpensive and safe. However, the anode choices are still very limited and unqualified due to the poor compatibility of many metal/metal oxides with acids.

This work demonstrates metallic Sn with high capacity and low redox potential as anode to enhance the upper limit of acidic batteries. The high hydrogen evolution overpotential, multiple electron transfer reaction, and high-kinetic stripping/plating chemistry enable Sn to become unique anode candidate in acid. An interfacial alloying regulation approach is applied to improve the uniformity and reversibility of Sn anode, thus achieving better performance and stability. Such Sn anode can also be coupled with various advanced cathodes to deliver promising performances.

at 4,000 C-rate.[17] On the other hand, the development of anode materials is falling behind in matching the advancement in the cathodes and gradually becoming the performance-limiting component for most, if not all, AABs.[18]

Traditional aqueous battery anode electrodes (metal oxides, metals, etc.) have poor compatibility with AABs since they may be dissolvable in acid. Among a few remaining anode options, the choices that can balance potential, kinetics, and capacity are very limited. As the most traditional anode, Pb undergoes a solid-state phase transition during the redox process, resulting in slow reaction kinetics and short lifespan.[8] Gas-type H_2/H^+ anode may bring better kinetics and lower polarization, but expensive long-lasting catalyst and heavy H_2 storage cell limited it from being further developed.[12] Recent efforts in intercalation-type materials like MoO_3 as the anodes provide more options in AABs.[19] Unfortunately, insufficient charge storage capacity (mainly <300 mAh g^{-1}) and intrinsically high redox potential (mainly >0 V vs. SHE) render these materials being difficult to meet the practical application requirements. Compared to other battery systems, metals with stripping/plating behavior (Li, Na, Zn, etc.) are considered the most promising solutions for anodes.[20,21] In principle, metal anodes have relatively high specific capacity and conductivity, as well as faster reaction kinetics due to the direct conversion of metal/metal ions.[22] However, apposite metal anode requires low redox potential (mainly below H_2/H^+), which is difficult to stabilize in electrolyte with relatively high concentration of protons.

High hydrogen evolution reaction (HER) overpotential and soluble ionic form are essential properties for the stable operation of stripping/plating metal anodes for AABs. Sn is a preferred choice because of its high HER overpotential in acidic environment, low redox potential below SHE, and soluble Sn^{2+} when oxidized.[23–25] Furthermore, it is relatively low-cost, non-toxic, and easy to recycle (Figure S1), making it a sustainable option.[26] With a body-centered tetragonal crystal structure and similar surface energy for facets, Sn metal deposits in polyhedral morphology isotropically and is less likely to form dendrite compared to Li or Zn.[27] However, large polyhedral Sn grains have limited contact with the substrate and are more likely to shed from the electrode and become "dead Sn" as the deposition capacity increases. The continuous formation of dead Sn and consequently the depletion of Sn ions in the electrolyte lower the battery performance leading to its eventual failure.

Here, we successfully demonstrate a high-capacity and high-reversibility Sn metal electrode as a universal anode choice for AABs via an interfacial copper alloying regulation approach. The copper substrate (Cu_s) is carefully selected from a variety of Sn-based alloys with the appropriate HER activity, inertness in acid, low toxicity, and cost effectiveness.[28–30] Both the experimental study and theoretical simulation show that the interfacial alloying significantly improved the reversibility, deposition uniformity, and inhibition of the metal shedding, leading to better electrochemical performance and stability. As a result, Sn/Cu_s depicts satisfactory specific capacity (~442 mAh g^{-1}), Coulombic efficiency (CE, ~98%), polarization (~11 mV at 2 mA cm^{-2}), and cycling durability (~93% CE after 300 cycles). To demonstrate its generality to the cathode medium, Sn anode was coupled with various cathode materials such as PbO_2, MnO_2, and polyaniline (PANI) to form a series of AABs. High output voltages (up to 1.7 V), superior specific energy densities (up to 312 Wh kg^{-1} based on both electrodes), fast kinetics (up to 93% charge/discharge capacity at 24 C), and long lifespans (up to 2,400 cycles) are achieved.

[1]MOE of the Key Laboratory of Bioinorganic and Synthetic Chemistry, The Key Lab of Low-carbon Chem & Energy Conservation of Guangdong Province, School of Chemistry, Sun Yat-sen University, Guangzhou, China

[2]Pritzker School of Molecular Engineering, The University of Chicago, Chicago, IL, USA

[3]Chemical Sciences and Engineering Division, Argonne National Laboratory, Lemont, IL, USA

[4]Department of NanoEngineering, University of California, San Diego, La Jolla, CA, USA

[5]Argonne Collaborative Center for Energy Storage Science (ACCESS), Argonne National Laboratory, Lemont, IL, USA

[6]Lead contact

*Correspondence: luxh6@mail.sysu.edu.cn (X.L.), shirleymeng@uchicago.edu (Y.S.M.)

https://doi.org/10.1016/j.joule.2023.04.011

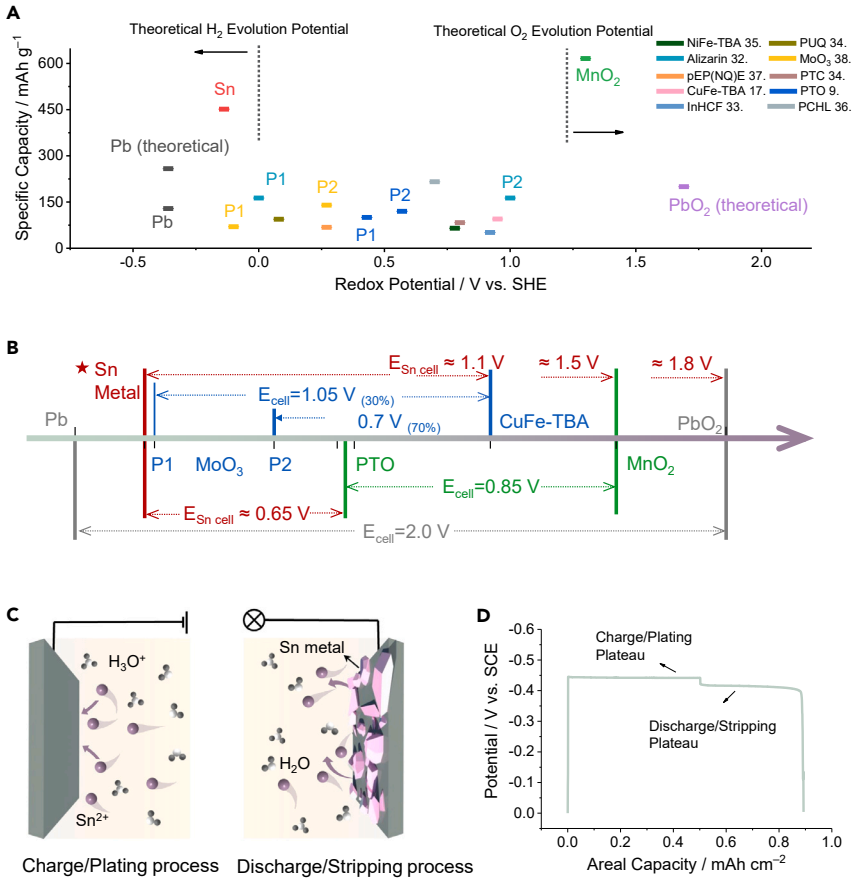

Figure 1. Sn electrode in aqueous acidic batteries

(A) Redox potentials and specific capacities of Sn metal anode and typically reported electrodes in AABs. P1 and P2 indicate the first and the second plateau.[9,17,32–38]

(B) Voltages of recently reported AAB devices and theoretical voltages of Sn-based cells.[9,38,39]

(C) Schematic illustration of the charge storage mechanism of the Sn anode in acidic electrolyte. The anions are omitted.

(D) Typical charge/discharge curve of Sn stripping/plating chemistry on graphite substrate at 2 mA cm^{-2}.

RESULTS

Potential analysis of Sn metal anode in aqueous acidic batteries

We selected various metals that may have stripping/plating behavior and reactivity near Pb electrode (Figure S2; Table S1).[31] Sn is the best choice based on Sn^{2+}/Sn redox couple at −0.14 V vs. SHE with a high electron storage capacity of 451.6 mAh g^{-1}. The high HER overpotential attributes its stability in acidic solution (Figure S3). These intrinsic advantages favor Sn in AAB systems (Figure 1A; Table S2).[9,17,32–38] As shown, the potentials of most electrodes are located at 0.2 to 1.0 V vs. SHE, limiting their matching options in full cell voltage. The Sn metal electrode is among the most negative and high-capacity electrodes, which can match with most electrodes (even some reported anodes) to achieve an output voltage higher than 0.5 V, up to 1.8 V. Details of voltage window matching diagram from recent published works in Figure 1B shows most of the full cell output voltages are below 1 V.[9,38,39] This unsatisfactory situation effectively ameliorated in the presence of Sn. Moreover, according to the φ-pH diagram for H_2O–Sn and previous studies, Sn^{2+} exists as soluble Sn ion precipitate in proton-enriched electrolyte, which

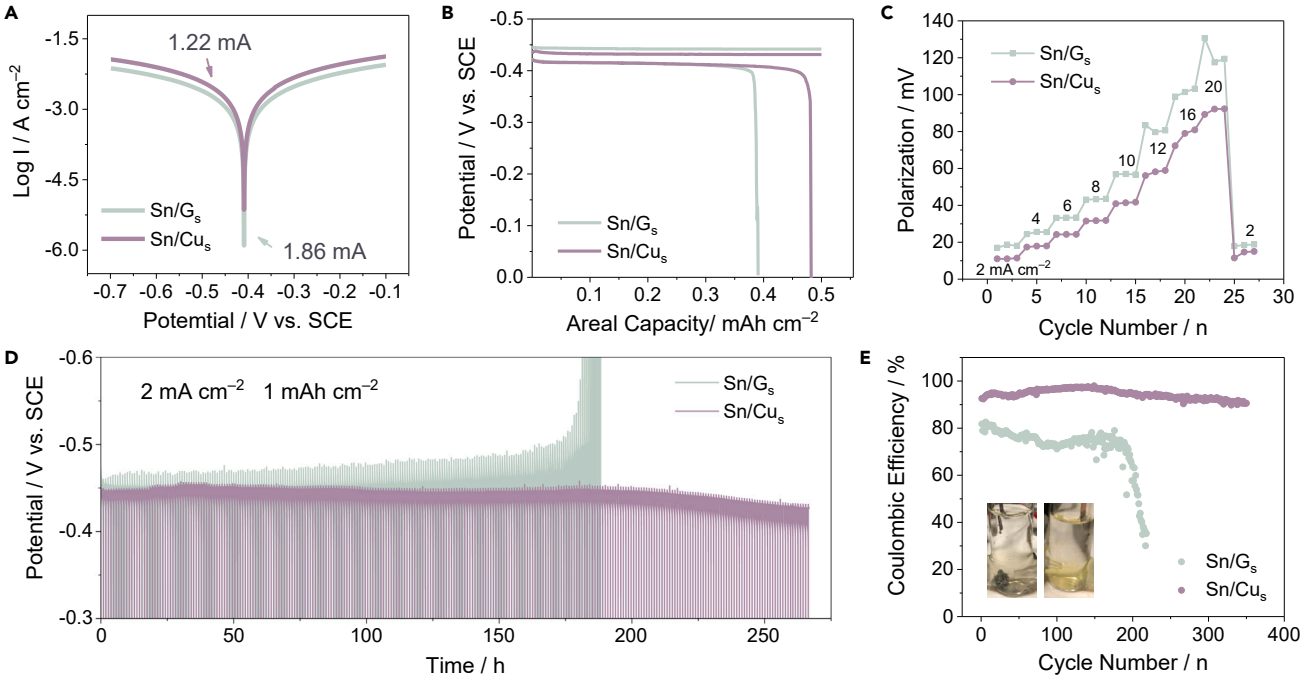

Figure 2. Electrochemical performance of Sn electrodes

(A) Corrosion curves of the Sn/G_s and Sn/Cu_s at 10 mV s^{-1}.

(B) Charge/discharge curves of Sn/G_s and Sn/Cu_s with a fixed charge capacity of 0.5 mAh cm^{-2} at 2 mA cm^{-2} after 25 cycles.

(C) Polarization profiles during continuous cycling at different current densities increasing from 2 to 20 mA cm^{-2} with a constant capacity of 0.5 mAh cm^{-2}.

(D and E) Magnified voltage profiles of Sn/G_s and Sn/Cu_s with a fixed charge capacity of 1 mAh cm^{-2} at 2 mA cm^{-2} (D) and corresponding CE (E). Inside are optical photographs after cycling test.

endows Sn metal functions to be more like the stripping/plating-type anodes with fast kinetics in AABs (Figure 1C).[40] Specific chemical behavior of Sn metal anode was studied by preliminary electrochemical test in 2 M H_2SO_4 and 0.1 M $SnSO_4$ electrolyte on graphite substrate (G_s). The voltage profiles in Figure 1D clearly exhibit a stable plateau at −0.42 V vs. SCE (saturated calomel electrode), which is consistent with the conversion of Sn^{2+}/Sn. The relatively low polarization reflects its superiority as an anode, but the CE of 78.5% is far lower than practical requirements, let alone after long cycling.

Electrochemical performance and characterization of Sn anodes

To achieve higher Coulombic efficiency of Sn anode, Cu_s was carefully selected to realize interfacial alloying regulation (Figure S4). The electrochemical performance of Sn anode on G_s and Cu_s (Figure S5) was studied in a three-electrode system under the same electrolyte used in the preliminary experiment. Figure 2A shows that Sn/Cu_s owns a lower corrosion current density, which is expected to suppress the corrosion rate and parasitic side reactions.[41] We then collected other indicators of Sn anode performance on different substrate via galvanostatic charge-discharge (GCD) method. A clearly longer discharge curve and near-theoretical capacity (~441.6 mAh g^{-1}) for Sn/Cu_s was observed (Figure 2B), corresponding to the higher CE and less irreversible capacity loss. Moreover, the polarization of Sn/Cu_s is reduced from 18.7 mV for Sn/G_s to 11 mV and is substantially smaller at different current densities from 2 to 20 mA cm^{-2} (Figure 2C). When the current density is switched back to 2 mA cm^{-2}, the voltage polarization changed little for Sn/Cu_s, suggesting a favorable stability.

To evaluate the stability, long-term cycling performance of Sn anodes were further measured at a current density of 2 mA cm^{-2} with a capacity limitation of 1 mAh cm^{-2} (Figures 2D and S6). As predicted by the preliminary experiment, the Sn/G_s electrode is trapped with larger voltage oscillations and drastically reduced charging plateau potential (especially after 100 h), which could be derived from electrode failure accompanied with the severe hydrogen evolution. In contrast, the Sn electrode based on Cu_s exhibits a more stable voltage profile along with a low polarization (~22 mV) even after cycling over 260 h. Furthermore, the corresponding CE of the voltage profiles in Figure 2E shows that Sn/Cu_s electrode presents a steady CE remaining at 91%–98% in 350 cycles, while Sn/G_s not only has a lower CE (~78%) at the very beginning but also continues to decline to less than 30% after cycling. Similar results were also found in other test conditions (Figure S7). Note, plenty of black insoluble Sn appears under Sn/G_s electrodes after cycling tests but not found in that for Sn/Cu_s. This phenomenon demonstrates that the dead Sn in Sn stripping/plating chemistry is successfully prohibited in Sn/Cu_s. The scientific nature of the Sn electrode design is also confirmed by investigating Sn stripping/plating behavior on Pt and Ni substrate (Figure S8). Sn shows similar redox peaks and voltage profile shape on all the substrates, but the cycling performance varies widely (Figure S9). As a stable substrate in acid, which can form alloy with Sn, Sn/Pt exhibits a competitive CE and lifespan with Sn/Cu_s. By contrast, the CE of Sn/Ni is much lower due to the reaction of nickel and acid. Linear sweep voltammetry results also show that the stability in acid is more important than HER activity. Under the comprehensive consideration of stability and price, Cu_s is proven to be a suitable choice for a highly reversible electrode, achieved by alloying. In addition, the thickness of Cu_s was found not to be decisive for performance. When the thickness of Cu_s increases from 20 μm to 400 μm, the electrochemical behavior (Figure S10) and cycling performance (Figure S11) have no significant changes. This can be attributed to the fact that the Sn-Cu alloying interaction only occurs at the interface, which will not cause significant impact on the substrate.

Sn anodes were further characterized to verify the presence of interfacial alloying. Typical polyhedron Sn particles were observed on both electrodes through scanning electron microscopy (SEM), but the ones on Sn/Cu_s have much smaller size and distribute more uniformly (Figure S12). The typical X-ray diffraction (XRD) patterns of the Sn anodes at different electrochemical states are presented in Figure S13. A stripping/plating mechanism is verified through the Sn signal, which raises at charged state and disappears at discharged state. In addition, the form of Sn metal is confirmed to be β-Sn (JCPDS#04-0673) with a body-centered tetragonal crystal structure in both electrodes from Figure 3A.[27] Except for the peaks from graphite (JCPDS#41-1487) and Cu (JCPDS#01-1242) substrates, no extraneous peaks appear in either pattern, proving that the Sn anode is free of impurities. The corresponding magnified XRD patterns of facet (200) and (101) were detailed analyzed in Figure 3B. Sn/Cu_s shows significantly larger full width at half maximum (FWHM) values than Sn/G_s, which could be assigned to a smaller average crystallite size of Sn metal based on Scherrer equation, consistent with previous visual results in Figure S12.[42] Besides, note that the position of two peaks corresponding to the facet spacing shifts toward positive of Sn/Cu_s, indicating a reduced facet distance according to Bragg's law. This can be attributed to the lattice shrinkage caused by the incorporation of copper atoms with smaller atomic radius into Sn lattice (1.35 vs. 1.45 Å), thus proving the existence of interfacial alloying.[43,44]

Relevant alloying interaction was further studied by chemical state via X-ray photoelectron spectroscopy (XPS). The existence of Sn (IV) was from the partial oxidization

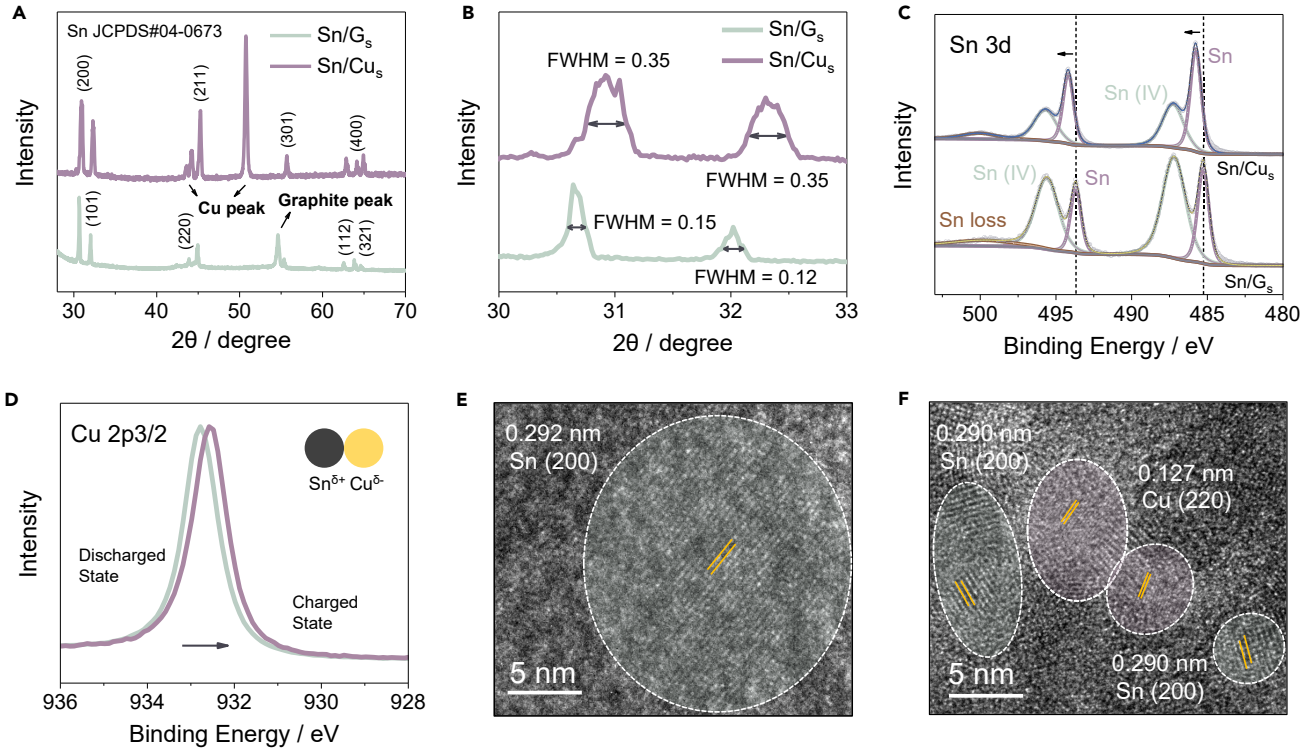

Figure 3. Material characterizations of Sn electrodes with/without alloying regulating

(A and B) XRD patterns (A) and part of XRD patterns (B) of Sn/G$_s$ and Sn/Cu$_s$.

(C) Sn 3d XPS spectra of Sn/G$_s$ and Sn/Cu$_s$.

(D) Cu 2p$_{3/2}$ spectra of Sn/Cu$_s$ at charged/discharged states.

(E and F) HRTEM images of Sn/G$_s$ (E) and Sn/Cu$_s$ (F).

of tin anode during the sample preparation (Figure 3C). Sn 3d XPS spectra also reveals a ~0.5 eV positive shift of Sn peak from Sn/G$_s$ to Sn/Cu$_s$, indicating Sn metal may have charge transfer with Cu$_s$.[45,46] It is further proven by high-resolution Cu 2p$_{3/2}$ spectra in Figure 3D, which shows a ~0.2 eV-lower binding energy in Sn/Cu$_s$ at fully charged state rather than discharged. It is reasonable due to the greater electronegativity of metallic Cu comparing with Sn (1.85 vs. 1.82), attracting electrons on the surface of Sn and exists in Sn$^{δ+}$/Cu$^{δ-}$ states.[47] In comparison, no significant shift is observed in C 1s spectra from Sn/G$_s$ (Figure S14). High-resolution transmission electron microscope (HRTEM) images Figures 3E and 3F reveal both (200) from β-Sn (JCPDS#04-0673) and (220) from Cu (JCPDS#01-1242) that are seen in Sn/Cu$_s$, with an interplanar spacing decrease of Sn (200), which is consistent with XRD results. In addition, the interfacial alloying was testified by the scanning transmission electron microscopy (STEM) and corresponding energy dispersive X-ray spectroscopy (EDS) elemental mapping (Figure S15). Homogeneous distribution of Cu and Sn is observed in Sn/Cu$_s$, while the distribution of C and Sn in Sn/G$_s$ is independent of each other. The alloying interface with a thickness of ~0.5 μm was also observed by SEM EDS mapping of side-view Sn/Cu$_s$ electrode (Figure S16), and Cu mass in the alloying interface remained nearly unchanged when the deposition capacity increased (Figure S17).

Insights into high Sn reversibility

The influence of interfacial alloying on reversible Sn deposition electrochemistry was further investigated. The morphology evolution study was first conducted through

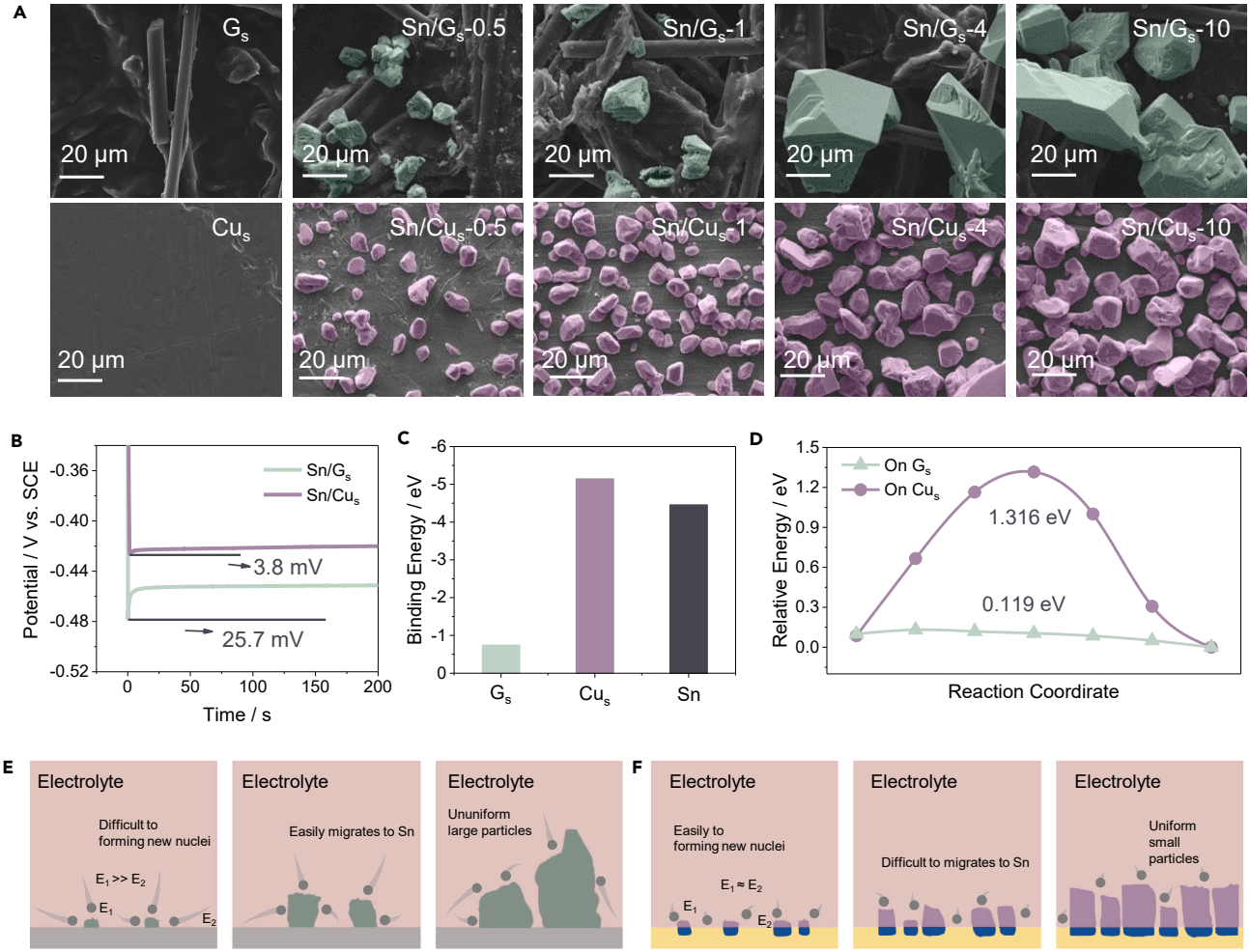

Figure 4. Study of interfacial regulation during Sn deposition process

(A) SEM images for Sn deposition on G_s and Cu_s substrates with different deposition capacities from 0.5 to 10 mAh cm^{-2}.

(B) The voltage-time curves during Sn nucleation at 2 mA cm^{-2} on G_s and Cu_s electrodes.

(C) The calculated binding energy of Sn^{2+}.

(D) The activation energy for migration of Sn^{2+} ion from one energy minima to the other nearby minima on C (002), Cu (220), and Sn (200).

(E and F) Illustration of the Sn metal deposition process on G_s (E) and Cu_s (F) substrate. Blue area means the interfacial alloying interaction. E_1 and E_2 mean the absolute value of binding energy on Sn seed and substrate, respectively.

ex situ SEM characterizations (Figure 4A). In the initial nucleation process, more Sn nuclei are observed in Sn/Cu_s, and the nucleation number keeps increasing during the deposition process. In contrast, the Sn grains in Sn/G_s prefer to grow over a few existing crystal nuclei rather than forming new ones. As a result, Sn polyhedron particles on G_s are substantially larger and uneven with very limited contact on substrate, whereas the metallic particles on Cu_s are relatively small and uniform even at a capacity of 10 mAh cm^{-2}. The real-time interface image was also acquired at different stages during Sn plating process (Figure S18). Several visible spots appeared after deposition for 10 min on Sn/G_s, and the growth of particles boomingly evolved and triggered a self-amplification behavior with the increase of the deposition time. By contrast, Sn/Cu_s showed a smooth surface during the whole plating process, which is consistent with the SEM results. To better understand the reason behind this difference, the voltage-time curves were collected to measure the overpotential during Sn nucleation. The nucleation overpotential indicates the gap

between the voltage extremum of the sharp voltage dropping and equilibrium plating potential at the beginning of the deposition process.[48] Smaller nucleation overpotential can be construed as an easier nucleation process in thermodynamics for subsequent crystal growth.[49] The result shows both electrodes undergo quick voltage dips corresponding to the nucleation process, but the overpotential of Sn/Cu_s (3.8 mV) is remarkably lower than that of Sn/G_s (25.7 mV) (Figure 4B). Such a dramatic difference illustrates the impact of interfacial alloying interaction in reducing the resistance for Sn nucleation through enhanced number of nucleation sites.

We then simulated the adsorption and diffusion processes of Sn via the density functional theoretical (DFT) calculation (Figures S19 and S20). The binding energy of Sn on G_s, Cu_s, or Sn metal in Figure 4C indicates that there is only one weak interaction between Sn and C (002) with a high binding energy of −0.74 eV, while Cu (220) (−5.11 eV) has a significantly lower binding energy and is stronger than Sn (200) (−4.46 eV) due to the extra interaction. The Cu_s substrate also possesses more negative potential vs. Pt in a three-electrode system than G_s, which is more likely to have contact with the Sn^{2+} ion in the Helmholtz layer (Figure S21).[50] Lower binding energy of Cu enables Cu_s to alleviate the concentration gradient at the interface by adhering a certain amount of Sn^{2+}, thus promoting uniform electric field distribution. Moreover, higher electron density near Fermi level in Sn projected density of states (PDOS) of Sn/Cu_s is observed, which corresponds to a better electron transfer activity (Figure S22). We also calculated the diffusion energy barriers of Sn migration between the adjacent energy minima to another nearby minima (Figure 4D). The energy barrier of Sn diffusion is only 0.12 eV on G_s, revealing an essentially instantaneous Sn diffusion process. In contrast, Cu_s has the highest diffusion energy barrier of 1.32 eV, which plays an important role in uniform deposition process. The details on Sn metal deposition on G_s and Cu_s are illustrated in Figures 4E and 4F. Relatively low fraction of Sn nucleates on G_s in the beginning. During the continuous deposition, the subsequent Sn atoms prefer to grow on the existing nuclei rather than form a new one as the result of a much stronger Sn binding energy on Sn metal surface than G_s. In addition, the Sn ions near bare G_s surface are prone to continuously diffusing onto these Sn nuclei and the resultant tip effect even makes the process more prevalent, leading to ununiform large particles. On the contrary, Cu_s has a slightly stronger binding energy than Sn metal, so the deposited Sn is easier to form new nuclei and subsequently increases the nucleation sites. The larger energy barrier also impedes the migration of Sn ions to as-deposited Sn particles. When charged under the same capacity, Sn/Cu_s will form more homogeneous and smaller particles.

To confirm the origin of the stability, change, and deactivation process, a long-term charge/discharge profile was magnified to study the nucleation process during cycling (Figure 5A). The nucleation overpotentials of both Sn/G_s and Sn/Cu_s decrease during the second cycle compared with the first one, which can be assigned to the several Sn nuclei left on the substrate by incomplete discharge. Existing Sn nuclei make the following nucleation process easier and reflected in the reduced overpotential. However, the overpotential of Sn/G_s re-increases every few cycles throughout the test (Figure S23), indicating that Sn particles would fall off and become deactivated, thus requiring re-nucleation on the next charge. The accumulation of dead Sn in Sn/G_s and Sn concentration decrease would finally cause serious HER side reaction, leading to a dramatic reduction in CE and the electrode failure (Figure S24). Note that the overpotential of Sn/Cu_s remains nearly unchanged during cycling and the CE is slightly less than 100%, so the nuclei are well preserved

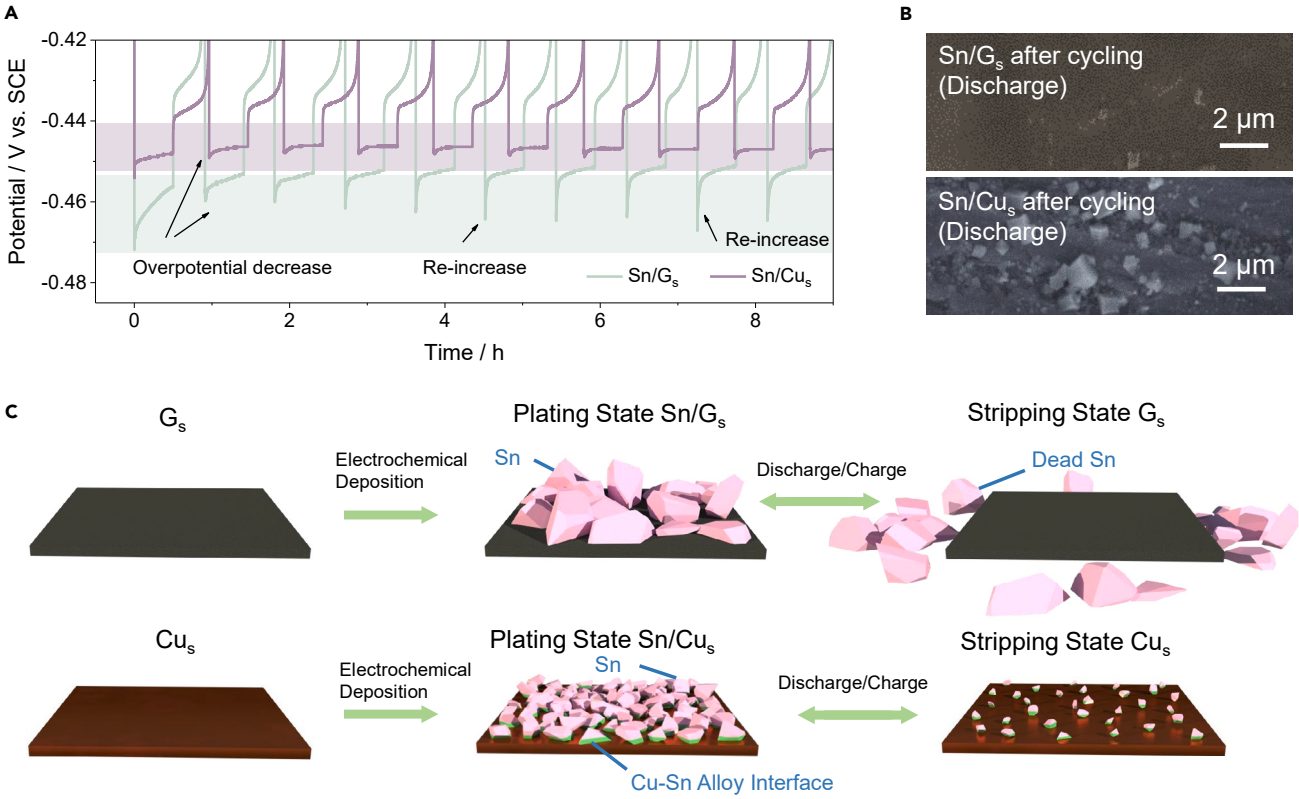

Figure 5. Investigation of cycling process

(A) Nucleation overpotential profile of first few cycles in Figure 2D.

(B) SEM images of Sn/G_s and Sn/Cu_s at discharged state after cycling test.

(C) Schematic illustration of the Sn stripping/plating chemistry on G_s and Cu_s substrates.

as the result of the increased interaction. This analysis was further proven by the SEM images of two electrodes after cycling (Figure 5B). Consequently, the Sn stripping/plating chemistry with interfacial alloying is summarized in Figure 5C. Alloying optimizes the deposition process and results in a better uniformity and reduced average crystallite size. The smaller polyhedron Sn particles along with enhanced interaction between Sn and substrate suppress the metal shedding during the charge/discharge process, thus improving the CE and cycling stability.

Performance of acidic Sn metal batteries

To further demonstrate the potential of Sn anode in energy storage applications, we assembled a series of advanced AAB devices by employing our Sn/Cu_s anode and representative cathodes of different mechanisms and redox potentials (Figure 6A). These aqueous acidic batteries with hybrid mechanisms are also known as "acidic tin metal batteries," similar to the nomenclature of other batteries with metal anode. These state-of-the-art tin metal battery devices (Figures 6B and S25; Table S3) have certain advantages over other recently reported acidic aqueous batteries.[8,9,33,34,36,38,51] PbO_2 as the most classic cathode was used for being among the ones with the highest potentials (Figure S26). PbO_2 undergoes $PbO_2/PbSO_4$ conversion reaction in this PbO_2//Sn battery system (Figure S27).[52] The GCD profile of our PbO_2//Sn cell at different current densities are shown in Figure 6C, which exhibits the full-cell discharge plateau of ~1.72 V. Although the output voltage is slightly lower than that of conventional lead-acid batteries, PbO_2//Sn batteries may achieve higher energy density under same cathode mass loading at reduced toxic Pb usage by calculation. In addition,

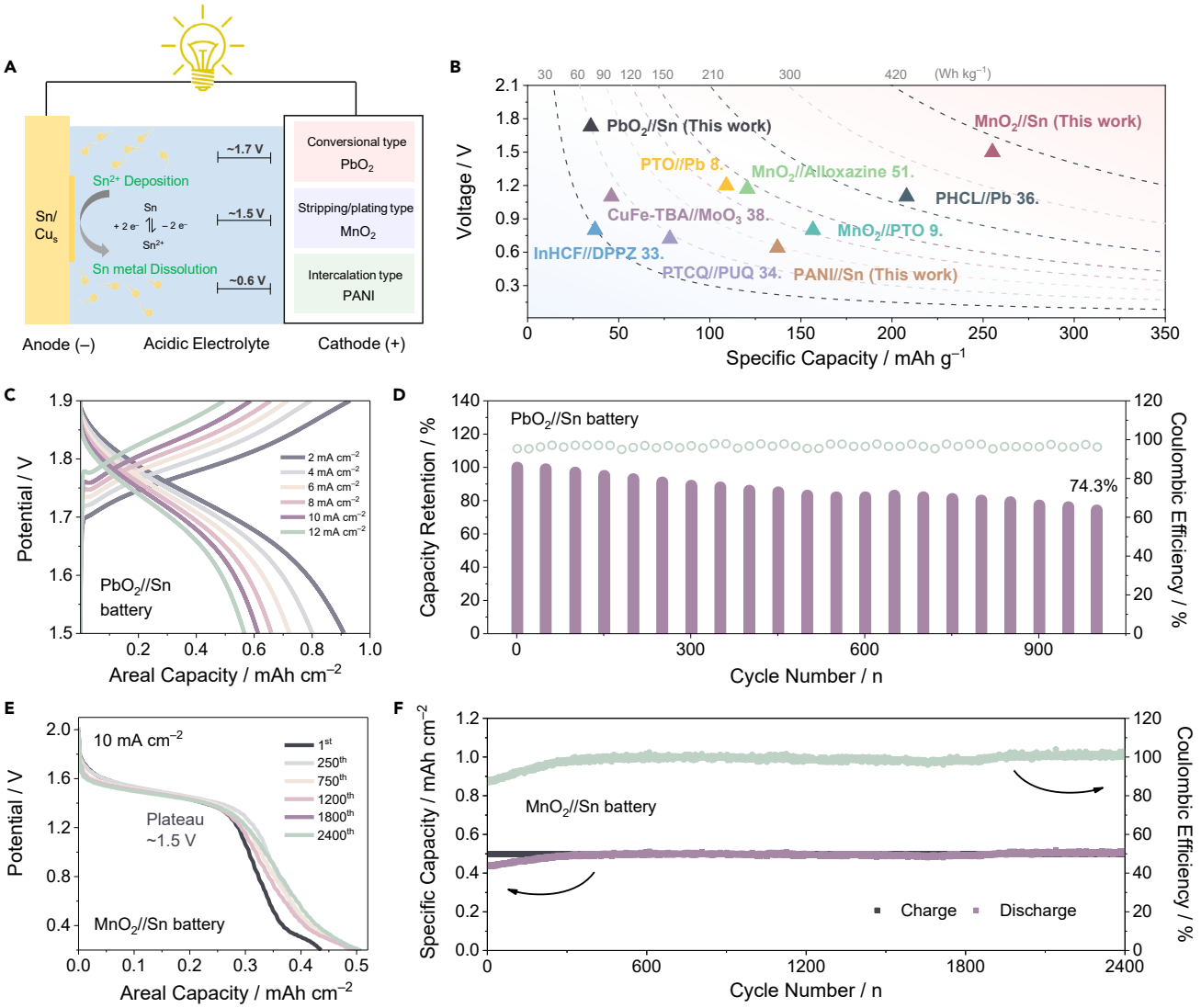

Figure 6. Electrochemical performance of acidic batteries based on Sn electrodes

(A) Schematics of AABs based on Sn/Cu$_s$ anode and cathodes with different mechanisms including PbO$_2$, MnO$_2$, and PANI.

(B) Cell voltage, area capacity, and energy density of three kinds of AABs comparing with other energy storage devices based on cathode and anode mass loading.[8,9,33,34,36,38,51]

(C and D) GCD curves at different current densities (C) and the cycling stability under 12 mA cm^{-2} (D) of PbO$_2$//Sn battery.

(E and F) Discharge curves at different cycles with a fixed charged capacity of 0.5 mAh cm^{-2} at 10 mA cm^{-2} (E) and long-term cycling performance at 10 mA cm^{-2} (F) of MnO$_2$//Sn battery.

PbO$_2$//Sn batteries have good rate capability (Figure S28) and durability of 74.3% capacity retention after 1,000 cycles (Figure 6D).

MnO$_2$//Sn batteries were also assembled to evaluate the advantages of Sn (Figures 6E and S29). MnO$_2$ is another important cathode with excellent electrochemical characteristics in AABs. However, the inadequate anode has dramatically restricted the potential and capacity of MnO$_2$ based AABs. Note that the stripping/plating-type MnO$_2$//Sn battery displayed a flat output voltage ~1.5 V at 2 mA cm^{-2} and a high voltage retention of more than 97.5% when current density reaches 12 mA cm^{-2} (Figure S30). Such a high discharge voltage considerably outstrips the previous MnO$_2$-based AABs. It also remains at 93% theoretical discharge

capacity under a charge capacity of 0.5 mAh cm^{-2} at 24C, proving its high-rate capability. The superhigh rate can be ascribed to the high kinetic of stripping/plating mechanism at both sides (Figure S31) and the good electroconductivity of Sn anode.[53] Note that the specific capacity, maximum energy density and power density based on the mass of both electrodes achieve 255.1 mAh g^{-1}, 312.2 Wh kg^{-1}, and 6.8 kW kg^{-1}, respectively. More energy density values based on different masses are also provided in Table S4 to provide more references. Moreover, our MnO_2//Sn battery shows long-cycling stability without obvious capacity decay at ~100% CE after 2,400 cycles (Figure 6F). The performance was also stable under the electrolyte-leaner conditions (Figure S32). Such promising battery performance parameters make MnO_2//Sn AABs a potential solution in the future grid-scale energy storage and daily transportation. To demonstrate the universality of Sn anode, we also used PANI cathode with intercalation-mechanism to form a PANI//Sn battery (Figure S33).[54] Although PANI has a low redox potential even reaching levels of some AAB anodes (like PTO, pyrene-4,5,9,10-tetraone), the battery is still able to deliver a voltage ~0.64 V, a high-rate capability (51% capacity retention from 2 to 20 mA cm^{-2}) and a good stability (82.7% capacity retention after 1,600 cycles) (Figure S34). Therefore, the Sn/Cu_s anode can adapt to various AAB cathodes with different mechanisms to form high-performance devices.

DISCUSSION

This study demonstrates a promising Sn metal anode with low redox potential, high capacity, and long durability for the application in AABs with enhanced output voltage, rate performance, and energy densities. The critical dead Sn issue is well prohibited by copper-tin interfacial alloying regulating, which results in high CE and long calendar life of Sn/Cu_s anode. For one thing, propensity for nucleation and higher Sn migration energy barrier lead to more uniform Sn deposition layer at reduced grain size. For another, extra interfacial interaction suppresses shedding of Sn polyhedron particles, thus enabling reversible stripping/plating chemistry. Benefiting from Sn/Cu_s anode and intrinsic advantages of proton-based batteries, we obtain various AABs with high performance by coupling Sn and advanced cathodes, forming a more diverse battery system. Especially MnO_2//Sn battery provides us a new potential choice for energy storage with excellent energy/power densities and service life. There is still much to explore in Sn-based AABs, like searching new electrolyte components, building 3D structure substrates for higher loading, further inhibiting the competition reaction of hydrogen evolution, and optimizing tin recycling process to reduce costs, but the development of promising Sn anode in this work will be immediately beneficial for the competitiveness of AABs as a next-generation choice for energy storage.

EXPERIMENTAL PROCEDURES

Resource availability

Lead contact

Further information and requests for resources should be directed to and will be fulfilled by the Lead Contact, Ying Shirley Meng (shirleymeng@uchicago.edu).

Materials availability

This study did not generate new unique reagents.

Data and code availability

This study did not generate any datasets.

Methods

Preparation of substrates and electrolytes

All the chemicals were of analytical grade and used directly without any purification. G_s and Cu_s were derived directly from graphite paper (0.5 cm × 2 cm × 0.04 cm) and pure Cu sheet (0.5 cm × 2 cm × 0.04 cm), respectively. Before use, Cu_s, Pt, and Ni were pretreated with hydrochloric acid and then washed with acetone and ethanol for 15 min to purify the surface. The G_s was also rinsed with ethanol to increase its hydrophilicity prior to experiments. For electrolyte, 1.074 g of stannous sulfate ($SnSO_4$) was added into 50 mL 2 M H_2SO_4 to prepare the mixed electrolyte of 2 M H_2SO_4 and 0.1 M $SnSO_4$.

Preparation of cathode materials—PbO_2, PANI, and MnO_2

PbO_2 was synthesized using a modified method reported in reference. PbO_2 was loaded on a piece of graphite paper (0.5 cm × 2 cm × 0.04 cm) by electrodeposition in a typical three-electrode setup on a CHI 760 electrochemical workstation with a constant voltage of 2.4 V for 700 s. The electrodeposition electrolyte is an aqueous solution containing 0.5 M $Pb(NO_3)_2$ and 1 M HNO_3. The three-electrode cell system was assembled with graphite paper as the working electrode and a carbon rod and a saturated calomel electrode (SCE) were used as the counter and reference electrodes, respectively. The mass loading of as-obtained PbO_2 electrode is 24.1 mg cm^{-2}.

PANI was synthesized using a modified method reported in our previous study. PANI was also plated onto carbon cloth (CC, 0.5 cm × 2 cm × 0.04 cm) by electrodeposition. This process was performed in a three-electrode system with cleaned CC, a carbon rod, and a SCE as the working electrode, the counter, and reference electrodes, respectively. The electrodeposition solution consisted of 1 M H_2SO_4 and 0.1 M aniline monomer. This electrodeposition was conducted by running a CV test at 10 mV s^{-1} with a voltage range from 0 to 1 V for 1 h. The mass loading of as-obtained PANI electrode is 1.5 mg cm^{-2}.

MnO_2 was electrodeposited onto graphite paper (0.5 cm × 2 cm × 0.04 cm) in a conventional three-electrode setup using Neware battery system (CT-3008-5V10mA-164, Shenzhen, China) on 1.4 V (vs. SCE) for 0.5 mAh cm^{-2}. The mass loading of the material is 0.81 mg cm^{-2}. Before electrodeposition, 0.3 M H_2SO_4 and 2 M $MnSO_4$ were prepared as the electrodeposition solution.

Electrochemical measurements

GCD curves, electrochemical impedance spectroscopy (EIS), and cyclic voltammogram (CV) were recorded by Neware battery system (CT-3008-5V10mA-164, Shenzhen, China) and electrochemical workstation (CHI 760E) under 25°C. In order to measure the electrochemical plating/stripping behaviors of Sn/Sn^{2+}, G_s and Cu_s substrates with a surface area of 0.5 cm^2 were used as working electrode, a graphite rod was employed as counter electrode, and SCE was the reference electrode in a three-electrode system with 20 mL electrolyte. The electrolyte is a mixed solution of 2 M H_2SO_4 and 0.1 M $SnSO_4$. The aqueous PbO_2//Sn and PANI//Sn were tested in two-electrode system in the electrolyte of 2 M H_2SO_4 and 0.1 M $SnSO_4$.

For the pouch cell demonstration, all used electrodes (2 cm × 1 cm) were the same as the previous tests. The electrolyte volume is 1 mL per cell. The pouch cells were assembled and sealed by the vacuum sealer. These pouch cells were tested under the same condition as the flooded cells. The voltage profiles can be found in Figure S35.

Preparation of electrolyte and measurement conditions of MnO_2//Sn cell

2.1477 g of $SnSO_4$ and 33.802 g manganese (II) sulfate monohydrate ($MnSO_4 \cdot H_2O$) were dissolved in 100 mL 0.3 M H_2SO_4, resulting in a mixture of 0.3 M H_2SO_4, 2 M $MnSO_4$, and 0.1 M $SnSO_4$. For MnO_2//Sn cell assembly, G_s and Cu_s were used as the anode with a surface area of 0.5 cm^2, and the graphite paper coated with MnO_2 was employed as the cathode in a two-electrode system. The N/P ratio by mass is ~1.4. The charging process was conducted by a constant voltage (2.1 V) method to charge a certain value, and the discharging process was inclined to 0 V by a galvanostatic discharging method after activation. The electrolyte-leaner MnO_2//Sn cell was tested using an acrylic box. The electrode area was 1 cm^2, and the electrolyte volume was 1 mL.

Characterizations

The electron micrographic structures of the deposited Sn on the substrates were characterized by Field-emission SEM (SEM, JSM-6330F, and SEM, g-500) and TEM (FEI Tecnai G2 F30). The crystalline structures and composition analysis of the precipitates were investigated by XPS (NEXSA, Thermo FS), FTIR (Nicolet/Nexus 670), and XRD (D-MAX 2200 VPC, RIGAKU). XPS was performed by using Al K Alpha source gun (hv = 1486.6 eV), an energy step size of 0.05 eV, and a pass energy of 40 eV. For XPS test, the capacity was controlled at 0.1 mAh cm^{-2} for Sn/Cu alloy surface investigation.

DFT calculation

All the calculations were carried out with DFT performed using the VASP program package. The generalized gradient approximation (GGA) in the scheme of Perdew-Burke-Ernzerhof (PBE) function was used to calculate the electron exchange-correlation interactions. A 400.0 eV cut-off energy was used for plane-wave basis set. All atomic positions and lattice vectors were fully optimized using a conjugate gradient algorithm to obtain the unstrained configuration. The convergence criterion for the structural optimizations was performed until the change of total energy was less than 1×10^{-5} eV, and all the forces on each atom were smaller than 0.01 eV/Å. All the structures were optimized with the Monkhorst-Pack K-point grid. The 4 × 4 × 1, 3 × 3 × 1, and 3 × 4 × 1 K-points were adopted to Sn (200), Cu (220), and C (002) planes, respectively. A vacuum space of 10 Å was placed along the z axis to avoid the interaction among the slabs. To find the transition states, nudged elastic band (NEB) method was used to study the minimum energy pathway of the diffusion of Sn metal on the surface.

SUPPLEMENTAL INFORMATION

Supplemental information can be found online at https://doi.org/10.1016/j.joule.2023.04.011.

ACKNOWLEDGMENTS

This work was supported by Guangdong province innovation and strong school project (2020ZDZX2004) and Joint Science Foundation of Wuyi University and HK and Macao (2019WGALH14). Y.S.M. acknowledges funding support from the Zable Endowed Chair of Energy Technology and the Sustainable Power & Energy Center (SPEC) of UC San Diego.

AUTHOR CONTRIBUTIONS

H.Z., X.L., and Y.S.M. conceived the idea and designed the project. H.Z. and D.X. performed the experimental work and analyzed the data. F.Y. carried out and interpreted the DFT calculations. J.X. and Q.L. helped with the cathode synthesis. D.-J.L.

and M.Z. contributed to the important discussion. H.Z. prepared the manuscript with input from all co-authors. Y.S.M. and X.L. supervised the project. All authors discussed the results and approved the final version of the manuscript.

DECLARATION OF INTERESTS

The authors declare no competing interests.

INCLUSION AND DIVERSITY

We support inclusive, diverse, and equitable conduct of research.

Received: October 31, 2022
Revised: February 28, 2023
Accepted: April 25, 2023
Published: May 17, 2023

REFERENCES

1. Rockström, J., Gaffney, O., Rogelj, J., Meinshausen, M., Nakicenovic, N., and Schellnhuber, H.J. (2017). A roadmap for rapid decarbonization. Science *355*, 1269–1271.
2. Bauer, C., Burkhardt, S., Dasgupta, N.P., Ellingsen, L.A.-W., Gaines, L.L., Hao, H., Hischier, R., Hu, L., Huang, Y., Janek, J., et al. (2022). Charging sustainable batteries. Nat. Sustain. *5*, 176–178.
3. Dunn, B., Kamath, H., and Tarascon, J.-M. (2011). Electrical energy storage for the grid: A battery of choices. Science *334*, 928–935.
4. Ji, X. (2021). A perspective of $ZnCl_2$ electrolytes: The physical and electrochemical properties. eScience *1*, 99–107.
5. Turcheniuk, K., Bondarev, D., Singhal, V., and Yushin, G. (2018). Ten years left to redesign lithium-ion batteries. Nature *559*, 467–470.
6. Liang, Y., Dong, H., Aurbach, D., and Yao, Y. (2020). Current status and future directions of multivalent metal-ion batteries. Nat. Energy *5*, 646–656.
7. Han, D., Cui, C., Zhang, K., Wang, Z., Gao, J., Guo, Y., Zhang, Z., Wu, S., Yin, L., Weng, Z., et al. (2021). A non-flammable hydrous organic electrolyte for sustainable zinc batteries. Nat. Sustain. *5*, 205–213.
8. Liang, Y., Jing, Y., Gheytani, S., Lee, K.Y., Liu, P., Facchetti, A., and Yao, Y. (2017). Universal quinone electrodes for long cycle life aqueous rechargeable batteries. Nat. Mater. *16*, 841–848.
9. Guo, Z., Huang, J., Dong, X., Xia, Y., Yan, L., Wang, Z., and Wang, Y. (2020). An organic/inorganic electrode-based hydronium-ion battery. Nat. Commun. *11*, 959.
10. Liang, G., Mo, F., Ji, X., and Zhi, C. (2020). Non-metallic charge carriers for aqueous batteries. Nat. Rev. Mater. *6*, 109–123.
11. Lopes, P.P., and Stamenkovic, V.R. (2020). Past, present, and future of lead–acid batteries. Science *369*, 923–924.
12. Chen, W., Li, G., Pei, A., Li, Y., Liao, L., Wang, H., Wan, J., Liang, Z., Chen, G., Zhang, H., et al. (2018). A manganese–hydrogen battery with potential for grid-scale energy storage. Nat. Energy *3*, 428–435.
13. Wang, X., Bommier, C., Jian, Z., Li, Z., Chandrabose, R.S., Rodríguez-Pérez, I.A., Greaney, P.A., and Ji, X. (2017). Hydronium-ion batteries with perylenetetracarboxylic dianhydride crystals as an electrode. Angew. Chem. Int. Ed. *56*, 2909–2913.
14. Emanuelsson, R., Sterby, M., Strømme, M., and Sjödin, M. (2017). An all-organic proton battery. J. Am. Chem. Soc. *139*, 4828–4834.
15. Zhou, L., Liu, L., Hao, Z., Yan, Z., Yu, X.-F., Chu, P.K., Zhang, K., and Chen, J. (2021). Opportunities and challenges for aqueous metal-proton batteries. Matter *4*, 1252–1273.
16. Zhong, C., Liu, B., Ding, J., Liu, X., Zhong, Y., Li, Y., Sun, C., Han, X., Deng, Y., Zhao, N., and Hu, W. (2020). Decoupling electrolytes towards stable and high-energy rechargeable aqueous zinc–manganese dioxide batteries. Nat. Energy *5*, 440–449.
17. Wu, X., Hong, J.J., Shin, W., Ma, L., Liu, T., Bi, X., Yuan, Y., Qi, Y., Surta, T.W., Huang, W., et al. (2019). Diffusion-free Grotthuss topochemistry for high-rate and long-life proton batteries. Nat. Energy *4*, 123–130.
18. Li, J., Yan, H., Xu, C., Liu, Y., Zhang, X., Xia, M., Zhang, L., and Shu, J. (2021). Insights into host materials for aqueous proton batteries: structure, mechanism and prospect. Nano Energy *89*, 106400.
19. Wang, X., Xie, Y., Tang, K., Wang, C., and Yan, C. (2018). Redox chemistry of molybdenum trioxide for ultrafast hydrogen-ion storage. Angew. Chem. Int. Ed. *57*, 11569–11573.
20. Liu, J., Bao, Z., Cui, Y., Dufek, E.J., Goodenough, J.B., Khalifah, P., Li, Q., Liaw, B.Y., Liu, P., Manthiram, A., et al. (2019). Pathways for practical high-energy long-cycling lithium metal batteries. Nat. Energy *4*, 180–186.
21. Zhao, Q., Stalin, S., and Archer, L.A. (2021). Stabilizing metal battery anodes through the design of solid electrolyte interphases. Joule *5*, 1119–1142.
22. Zhang, H., Liu, Q., Zheng, D., Yang, F., Liu, X., and Lu, X. (2021). Oxygen-rich interface enables reversible stibium stripping/plating chemistry in aqueous alkaline batteries. Nat. Commun. *12*, 14.
23. Li, Q., Wang, Y., Mo, F., Wang, D., Liang, G., Zhao, Y., Yang, Q., Huang, Z., and Zhi, C. (2021). Calendar life of Zn batteries based on Zn anode with Zn powder/current collector structure. Adv. Energy Mater. *11*, 2003931.
24. Azizi, O., Jafarian, M., Gobal, F., Heli, H., and Mahjani, M.G. (2007). The investigation of the kinetics and mechanism of hydrogen evolution reaction on tin. Int. J. Hydrogen Energy *32*, 1755–1761.
25. Wei, L., Jiang, H.R., Ren, Y.X., Wu, M.C., Xu, J.B., and Zhao, T.S. (2019). Investigation of an aqueous rechargeable battery consisting of manganese tin redox chemistries for energy storage. J. Power Sources *437*, 226918.
26. Wang, G., Aubin, M., Mehta, A., Tian, H., Chang, J., Kushima, A., Sohn, Y., and Yang, Y. (2020). Stabilization of Sn anode through structural reconstruction of a Cu-Sn intermetallic coating layer. Adv. Mater. *32*, 2003684.
27. Yao, Y., Wang, Z., Li, Z., and Lu, Y.C. (2021). A dendrite-free tin anode for high-energy aqueous redox flow batteries. Adv. Mater. *33*, 2008095.
28. Tu, Z., Choudhury, S., Zachman, M.J., Wei, S., Zhang, K., Kourkoutis, L.F., and Archer, L.A. (2018). Fast ion transport at solid–solid interfaces in hybrid battery anodes. Nat. Energy *3*, 310–316.
29. Zhang, Y., Howe, J.D., Ben-Yoseph, S., Wu, Y., and Liu, N. (2021). Unveiling the origin of alloy-seeded and nondendritic growth of Zn for rechargeable aqueous Zn batteries. ACS Energy Lett. *6*, 404–412.
30. Liang, S., Cheng, Y.J., Zhu, J., Xia, Y., and Müller-Buschbaum, P. (2020). A chronicle review of nonsilicon (Sn, Sb, Ge)-based lithium/sodium-ion battery alloying anodes. Small Methods *4*, 2000218.

31. Bratsch, S.G. (1989). Standard electrode potentials and temperature coefficients in water at 298.15 K. J. Phys. Chem. Ref. Data *18*, 1–21.

32. Tong, L., Jing, Y., Gordon, R.G., and Aziz, M.J. (2019). Symmetric all-quinone aqueous battery. ACS Appl. Energy Mater. *2*, 4016–4021.

33. Qiao, J., Qin, M., Shen, Y.M., Cao, J., Chen, Z., and Xu, J. (2021). A rechargeable aqueous proton battery based on a dipyridophenazine anode and an indium hexacyanoferrate cathode. Chem. Commun. *57*, 4307–4310.

34. Zhu, M., Zhao, L., Ran, Q., Zhang, Y., Peng, R., Lu, G., Jia, X., Chao, D., and Wang, C. (2022). Bioinspired catechol-grafting PEDOT cathode for an all-polymer aqueous proton battery with high voltage and outstanding rate capacity. Adv. Sci. *9*, 2103896.

35. Wu, X., Qiu, S., Xu, Y., Ma, L., Bi, X., Yuan, Y., Wu, T., Shahbazian-Yassar, R., Lu, J., and Ji, X. (2020). Hydrous nickel-iron turnbull's blue as a high-rate and low-temperature proton electrode. ACS Appl. Mater. Interfaces *12*, 9201–9208.

36. Yue, F., Tie, Z., Deng, S., Wang, S., Yang, M., and Niu, Z. (2021). An ultralow temperature aqueous battery with proton chemistry. Angew. Chem. Int. Ed. *60*, 13882–13886.

37. Strietzel, C., Sterby, M., Huang, H., Strømme, M., Emanuelsson, R., and Sjödin, M. (2020). An aqueous conducting redox-polymer-based proton battery that can withstand rapid constant-voltage charging and sub-zero temperatures. Angew. Chem. Int. Ed. *59*, 9631–9638.

38. Jiang, H., Shin, W., Ma, L., Hong, J.J., Wei, Z., Liu, Y., Zhang, S., Wu, X., Xu, Y., Guo, Q., et al. (2020). A high-rate aqueous proton battery delivering power below −78 °C via an unfrozen phosphoric acid. Adv. Energy Mater. *10*, 2000968.

39. Ruetschi, P. (1977). Review on the lead—acid battery science and technology. J. Power Sources *2*, 3–120.

40. Zhou, X., Lin, L., Lv, Y., Zhang, X., and Wu, Q. (2018). A Sn-Fe flow battery with excellent rate and cycle performance. J. Power Sources *404*, 89–95.

41. Zhou, M., Guo, S., Li, J., Luo, X., Liu, Z., Zhang, T., Cao, X., Long, M., Lu, B., Pan, A., et al. (2021). Surface-preferred crystal plane for a stable and reversible zinc anode. Adv. Mater. *33*, 2100187.

42. Patterson, A.L. (1939). The Scherrer formula for X-ray particle sizedetermination. Phys. Rev. *56*, 978–982.

43. Slater, J.C. (1964). Atomic radii in crystals. J. Chem. Phys. *41*, 3199–3204.

44. Pei, Y., Zheng, L., Li, W., Lin, S., Chen, Z., Wang, Y., Xu, X., Yu, H., Chen, Y., and Ge, B. (2016). Interstitial point defect scattering contributing to high thermoelectric performance in SnTe. Adv. Electron. Mater. *2*, 1600019.

45. Jiang, X., Wang, X., Liu, Z., Wang, Q., Xiao, X., Pan, H., Li, M., Wang, J., Shao, Y., Peng, Z., et al. (2019). A highly selective tin-copper bimetallic electrocatalyst for the electrochemical reduction of aqueous CO_2 to formate. Appl. Catal. B Environ. *259*, 118040.

46. Vasileff, A., Zhi, X., Xu, C., Ge, L., Jiao, Y., Zheng, Y., and Qiao, S.-Z. (2019). Selectivity control for electrochemical CO_2 reduction by charge redistribution on the surface of copper alloys. ACS Catal. *9*, 9411–9417.

47. Mann, J.B., Meek, T.L., Knight, E.T., Capitani, J.F., and Allen, L.C. (2000). Configuration energies of the d-block elements. J. Am. Chem. Soc. *122*, 5132–5137.

48. Yan, K., Lu, Z., Lee, H.-W., Xiong, F., Hsu, P.-C., Li, Y., Zhao, J., Chu, S., and Cui, Y. (2016). Selective deposition and stable encapsulation of lithium through heterogeneous seeded growth. Nat. Energy *1*, 16010–16018.

49. Wang, H., Matios, E., Luo, J., and Li, W. (2020). Combining theories and experiments to understand the sodium nucleation behavior towards safe sodium metal batteries. Chem. Soc. Rev. *49*, 3783–3805.

50. Wang, F., Xie, J., Zheng, D., Yang, F., Zhang, H., and Lu, X. (2022). Intrinsic carbon defects induced reversible antimony chemistry for high-energy aqueous alkaline batteries. Adv. Mater. *34*, 2200085.

51. Sun, T., Du, H., Zheng, S., Shi, J., and Tao, Z. (2021). High power and energy density aqueous proton battery operated at −90 °C. Adv. Funct. Mater. *31*, 2010127.

52. Xu, Y., Cai, P., Chen, K., Ding, Y., Chen, L., Chen, W., and Wen, Z. (2020). High-voltage rechargeable alkali-acid Zn-PbO_2 hybrid battery. Angew. Chem. Int. Ed. *59*, 23593–23597.

53. Chao, D., Zhou, W., Ye, C., Zhang, Q., Chen, Y., Gu, L., Davey, K., and Qiao, S.Z. (2019). An electrolytic Zn-MnO_2 battery for high-voltage and scalable energy storage. Angew. Chem. Int. Ed. *58*, 7823–7828.

54. Wan, F., Zhang, L., Wang, X., Bi, S., Niu, Z., and Chen, J. (2018). An aqueous rechargeable zinc-organic battery with hybrid mechanism. Adv. Funct. Mater. *28*, 1804975.